Acta Materialia 227 (2022) 117695

Contents lists available at ScienceDirect

Acta Materialia

journal homepage: www.elsevier.com/locate/actamat

# On the mechanism of Mn(II)-doping in Scandia stabilized zirconia electrolytes

Einar Vøllestad[a,*], Vegar Øygarden[a], Joachim Seland Graff[a], Martin Fleissner Sunding[a], John D. Pietras[b], Jonathan M. Polfus[a], Marie-Laure Fontaine[a]

[a] Department of Sustainable Energy Technology, SINTEF Industry, Oslo, Norway
[b] Saint-Gobain R&D Center, Northborough, MA 01532, USA

ARTICLE INFO

*Article history:*
Received 9 August 2021
Revised 18 January 2022
Accepted 27 January 2022
Available online 29 January 2022

*Keywords:*
Electrical conductivity
SOFC
Reactive sintering
ScSZ
Stability

ABSTRACT

Cubic Scandia-stabilized zirconia (ScSZ) is an attractive electrolyte material for solid oxide cells due to its significant ionic conductivity, provided that the phase transition to its rhombohedral polymorph upon cooling is suppressed. The latter is achieved with addition of a secondary co-dopant, albeit it may be at the detriment of its ionic conductivity Here, we thoroughly investigate how $MnO_2$ (0.5–10 mol%) as a co-dopant impacts on the sinterability, thermal expansion, crystal structure and ionic conductivity of $ZrO_2$ doped with 10 mol% Scandia (10ScSZ), and we provide new insight on the chemistry of dissolved manganese in the fluorite lattice. Reactive sintering of 2 mol% $MnO_2$ mixed with 10ScSZ enables to produce dense electrolyte with significant reduction of the peak sintering temperature and stabilisation of the cubic structure down to room temperature. Combined density functional theory and X-ray photoelectron spectroscopy analyses reveal that manganese predominantly enters the structure as $Mn^{2+}$ during reactive sintering, with a prevalence of higher valence states at the surface and grain boundaries. The highest oxide ion conductivity is achieved for 2 mol% doped 10ScSZ (120 $mScm^{-1}$ at 800 °C) and it decreases with increasing Mn concentration. For all compositions, the bulk conductivity remains independent of $pO_2$ – corroborating a limited electronic conductivity contribution from Mn-doping. The grain boundary conductivity is found to decrease with sintering time and $pO_2$, which is attributed to the chemistry and concentration of segregated manganese at the surface and grain boundaries, yielding depletion of oxygen vacancies in the space charge layer.



## 1. Introduction

Solid Oxide Cells (SOCs) are electrochemical energy conversion devices operating with low emission of greenhouses gases as fuel cells (SOFC) for power generation, and as electrolysers (SOECs) for hydrogen production. Their reversible operation (rSOCs) is foreseen to provide an efficient energy storage solution for grid stabilisation and balancing energy production and consumption in an energy system dominated by intermittent energy sources. Conventional SOFCs operate at temperature typically ranging between 800 and 1000 °C using yttria-stabilised zirconia (YSZ) as the electrolyte, which exhibits excellent oxide ion conductivity in this temperature range (20–30 $mScm^{-1}$ for 8 mol% Y-doped $ZrO_2$ at 800 °C). However, these high temperatures challenge SOFCs durability, due to degradation of the cell components. Lowering the operation temperature to an intermediate range (600–800 °C) would improve cell durability and reduce both capital and operational costs. However, YSZ ionic conductivity dramatically decreases with temperature [1].

The search for alternative electrolyte materials operating below 750 °C has shown that combining substantial oxide ion conductivity with sufficient mechanical strength, high stability in both oxidizing and reducing conditions, ease of processing and low cost is a major challenge [2]. Sc-stabilised (6–12 mol% $Sc_2O_3$) $ZrO_2$ (ScSZ) has a higher ionic conductivity at intermediate temperatures (above 20 $mScm^{-1}$ at 600 °C) and is therefore a very attractive electrolyte material [3–6]. The high oxide ion conductivity of ScSZ is attributed to the small difference in ionic radius between $Zr^{4+}$ and $Sc^{3+}$ (0.84 Å and 0.87 Å, respectively, in 8-fold coordination), which reduces the degree of defect association and minimizes the barrier for oxygen vacancy migration in the fluorite

* Corresponding author.
*E-mail address:* Einar.vollestad@sintef.no (E. Vøllestad).

https://doi.org/10.1016/j.actamat.2022.117695

structure. However, the similarity of the ionic radii also limits the extent of structural stabilisation with respect to the phase transition around 550 °C from the highly conducting cubic phase to a rhombohedral phase exhibiting significantly lower conductivity [7,8]. This phase transition occurs due to ordering of the oxygen vacancies accompanied by a volume change and a decrease in vacancy mobility.

Several studies showed that co-doping with larger trivalent or tetravalent cations such as $Bi^{3+}$, $Gd^{3+}$, $Ce^{4+}$, $Y^{3+}$, $Yb^{3+}$, and $Sm^{3+}$ can suppress vacancy ordering and stabilize the cubic phase upon cooling to room temperature [2,6,7,9,10]. Among these, electrolyte co-doped with 1 mol% of $CeO_2$ has been shown to retain their high ionic conductivity towards intermediate temperatures (550–700 °C) while also requiring lower sintering temperature to reach high density [4,11]. However, the long-term stability of Ce-doped ScSZ under reducing conditions is challenged by the partial reduction of $Ce^{4+}$ to $Ce^{3+}$, with some reports showing conductivity degradation rates of 5–25%/khr for different operating conditions [3,12,13].

Manganese is an alternative and less explored co-dopant for SOC electrolyte. In its divalent state $Mn^{2+}$ presents a similar ionic radius to $Ce^{4+}$ in the cubic fluorite structure (0.96 Å in 8-fold coordination) [14,15]. It may offer several additional benefits: (i) $MnO_2$ has been reported to act as a sintering aid for many ceramics and may thus improve the sinterability of the electrolyte [16], (ii) a homogeneous concentration of manganese in the electrolyte is likely to reduce the driving force for Mn diffusion from Mn-containing electrodes [17], and (iii) small additions of manganese may be used to tailor the thermal expansion coefficient (TEC) of the electrolyte to better match the TEC of other key components in the cell. Nevertheless, the addition of a transition metal cation may also increase the electronic conductivity of the electrolyte [18].

Several studies have shown that small amounts of manganese co-doping in YSZ can stabilize the cubic polymorph at lower yttrium concentrations [14,19]. It has also been observed that Mn may partly segregate to the grain boundaries and influence the space charge regions and ultimately affect the grain boundary resistance of the ceramic [20].

While the tertiary phase diagram $Sc_2O_3$-$ZrO_2$-$MnO_2$ is not fully explored, a few studies reported that $MnO_2$ mixed with 10ScSZ or 11ScSZ at concentrations above 1.5 mol% enable to stabilize the cubic polymorph at room temperature [21,22,7]. In both compositions, the sinterability improved and the electrical conductivity was similar to that of 10ScSZ at 800 °C [15]. However, the defect and structural chemistry of manganese doping in ScSZ is not well described or understood, and the impact of redox cycling on the valence state of the manganese dopant and ultimately the electronic properties of ScSZ have not been addressed in details. Since $Mn^{2+}$ has a larger ionic radius than both $Zr^{4+}$ and $Sc^3$ (0.96 Å in 8-fold coordination), addition of excess $Mn^{2+}$ may result in an increased trapping and reduced mobility of oxygen vacancies in the fluorite structure. Potential Mn segregation to the grain boundaries and effect on space charge regions is also not explored for the Sc-doped zirconia system. Hence, more work is needed to understand the impact of Mn-doping in ScSZ and assess its potential as a SOC electrolyte material.

In this work, we investigate how the $MnO_2$ dopant concentration in 10ScSZ impacts the sinterability, thermal expansion, crystal structure and ionic conductivity. These studies are supported by in-depth chemical and structural characterisation using Transmission Electron Microscopy (TEM), X-Ray Photoelectron Spectroscopy (XPS) and Density Functional Theory (DFT) modelling to establish the valency of Mn in cubic ScSZ and its impact on the defect chemistry and ionic conductivity.

## 2. Methods

### 2.1. Powder and sample preparation

Stoichiometric amounts of 10 mol% $Sc_2O_3$ stabilised $ZrO_2$ (10ScSZ, Fuel Cell Materials) and $MnO_2$ (Sigma-Aldrich, >99%) powders were used to prepare the powder mixtures for reactive sintering. Several compositions were screened and noted as follows: undoped material (10ScSZ = 10 mol% $Sc_2O_3$ stabilised $ZrO_2$), 1MnScSZ for 1 mol% $MnO_2$ doped 10ScSZ, and similar notations for increased co-dopant: 2Mn10ScSZ, 4Mn10ScSZ, 6Mn10ScSZ and 10Mn10ScSZ. For initial screening of $MnO_2$-concentrations, the powders were dry-mixed using mortar and pestle. For the thorough investigation of 2 mol% $MnO_2$-doped ScSZ (2MnScSZ), the powders mixture was dispersed in isopropanol and planetary milled in a Retsch PM400 Planetary Mill at 150 rpm for 20 min. After evaporation of the solvent, the dried powders were pressed into green pellets of 20 mm diameter and sintered in a muffle furnace at 1250 °C-1500 °C for 5–20 h, with a heating rate of 3 °C/min and a cooling rate of 1.6 °C/min.

### 2.2. Sample characterization

Dilatometry measurements were performed using a NETZSCH DIL 402C/4/G push rod dilatometer upon annealing of 10 mm diameter pellets in stagnant air from room temperature (RT) to 1550 °C with both heating and cooling rates of 2 °C/min. Scanning Electron Microscopy (SEM) was performed on a Nova NanoSEM 650 FEG-SEM from FEI. Fractured cross-sections of the samples were observed using back-scattered electrons and a high tension of 5 kV.

X-ray diffraction (XRD) data on pellets and powders were collected at room temperature using Cu-radiation with a PANalytical Empyrean Alpha-1 instrument equipped with a PIXel$^{3D}$ detector. Data were collected in a $2\theta$-range of 15–90°. High-temperature XRD data were collected using an Anton Paar high-temperature stage equipped with a flat plate setup. Lattice parameters and weight fractions of polymorphs were extracted by the Rietveld-refinement method using the Topas v6.0 software. The fundamental parameter peak profile function was used to fit the peak profiles with basis in the instrument setup. Chebychev background polynomials with 5 terms were used to fit the background.

X-ray photoelectron spectroscopy (XPS) characterisation was performed on a Kratos Analytical AxisUltra$^{DLD}$ spectrometer using monochromatic Al K$\alpha$ X-rays and applying low energy electrons for charge compensation. The energy scale of the spectra was corrected based on the measured position of the Zr $3d_{5/2}$ peak which is well defined in these samples. It is set to 181.8 eV binding energy (BE) based on its average position after setting the C 1 s peak from adventitious carbon to 284.8 eV BE. Element quantification was based on the manufacturer's relative sensitivity factors.

The oxidation state of manganese was inferred from the Mn $2p_{3/2}$ peak shape. A Shirley background was subtracted from the experimental spectra before fitting the Mn $2p_{3/2}$ peak based on spectra obtained on pure oxides [23]. The determination of the Mn oxidation state was in addition attempted based on the multiplet splitting of the Mn 3 s peak [24] but the signal-to-noise intensities were too low to obtain satisfactory results.

### 2.3. DFT modelling

DFT calculations were carried out using projector-augmented wave pseudopotentials and the PBE0 hybrid functional as implemented in VASP [25,26]. The calculations were spin-polarized and the following valence electrons were included: Zr $4s^2p^6d^2\ 5s^2$; Mn $3s^2p^6d^5\ 4s^2$; O $2s^2p^4$. The plane wave energy cutoff was 400 eV

and k-point sampling was performed according to 4 × 4 × 4 Monkhorst-Pack grid for the cubic $Fm\bar{3}m$ unit cell. The ionic positions were relaxed within 0.02 eV Å$^{-1}$ and the optimized lattice parameter was 5.044 Å for undoped $ZrO_2$. The calculated band gap for the bulk $ZrO_2$ structure was 5.82 eV. Manganese substitution was considered in a 2 × 2 × 2 supercell (96 atoms) with fixed lattice parameters, corresponding to a dopant concentration of 3%. The effective charge state of the considered point defects was modified by adding or subtracting electrons which were compensated by a uniform background charge.

The Gibbs formation energy of fully ionized oxygen vacancies as function of temperature and oxygen partial pressure was calculated as

$$\Delta G^{\mathrm{f}}(T,p) = E^{\mathrm{tot}}_{\mathrm{def}} - E^{\mathrm{tot}}_{\mathrm{bulk}} + \mu_{\mathrm{O}}(T,p) + 2\mu_{\mathrm{e}} \quad (1)$$

where $E^{\mathrm{tot}}_{\mathrm{def}}$ and $E^{\mathrm{tot}}_{\mathrm{bulk}}$ are the total energies of the defective and bulk cells, respectively, $\mu_{\mathrm{O}}$ is the chemical potential of oxygen and $\mu_{\mathrm{e}}$ is the Fermi level. The entropy contribution from the solid phase was thereby assumed to be negligible relative to the gas phase. The chemical potential of oxygen was obtained according to

$$\mu_{\mathrm{O}}(T,p) = \mu^{\mathrm{o}}_{\mathrm{O}} + \mu_{\mathrm{O}}(T) + \mathrm{k}T\ln(p/p^{\mathrm{o}}) \quad (2)$$

where $\mu^{\mathrm{o}}_{\mathrm{O}} = \frac{1}{2}E^{\mathrm{tot}}_{\mathrm{O2}}$, and $\mu_{\mathrm{O}}(T)$ was obtained from thermochemical tables. Notably, the calculated binding energy of the $O_2$ molecule, −5.20 eV, was in good agreement with the experimental value, which otherwise can be a significant source of error with other functionals or methods. The equilibrium Fermi level at given conditions was determined by imposing the predominant electroneutrality condition according to

$$c(\mathrm{v}^{\bullet\bullet}_{\mathrm{O}}) = N\exp\left(\Delta G^{\mathrm{f}}/\mathrm{k}T\right) = \frac{1}{2}c\left(\mathrm{Sc}^{'}_{\mathrm{Zr}}\right) = 0.1 \quad (3)$$

where $N = 2$ for $\mathrm{v}^{\bullet\bullet}_{\mathrm{O}}$ in fluorites. The thermodynamic charge transition levels of $\mathrm{Mn}^{q}_{\mathrm{Zr}}$ were thereby evaluated in comparison to the equilibrium Fermi level in the system as a function of temperature and $p_{\mathrm{O_2}}$.

### 2.4. Electrical measurements

For the electrical characterisation of Mn-doped ScSZ pellets, composite electrodes of Pt/10ScSZ were applied by brush painting and annealed at 1050 °C for 2 h to produce symmetrical cells. The cells were mounted in a Probostat™ sample holder (NorECs, Norway) in a 4-wire 2-point setup using Pt wires. The conductivity was measured as a function of temperature using a Solartron 1260 FRA. Measurements were conducted in synthetic air, Ar and humidified 20% $H_2$/80% Ar (0.028 atm $H_2O$) with gas flows monitored using Bronkhorst mass flow controllers. Electrochemical impedance spectra were recorded after equilibration at each temperature – ensured by monitoring the impedance at 10 kHz during equilibration. EIS measurements were taken upon cooling, but individual values were reproduced upon heating at 600 °C, 700 °C and 800 °C before the atmosphere was changed at the highest temperatures.

## 3. Results

### 3.1. Sintering and microstructure of Mn-doped ScSZ

The sintering behaviour of three different samples (undoped 10 ScSZ, 1% and 2% mol% $MnO_2$ co-doped 10ScSZ) is illustrated in Fig. 1 showing the sintering rate corresponding to the derivative of the linear expansion during sintering as a function of temperature. Only a minor change was observed for the optimal shrinkage rate upon addition of 1 mol% $MnO_2$ compared to the undoped electrolyte, whereas a significant shift towards lower temperatures was seen with the addition of 2 mol% $MnO_2$. Accordingly, $MnO_2$ acts as an efficient sintering aid for 10ScSZ at concentrations above 1 mol%.

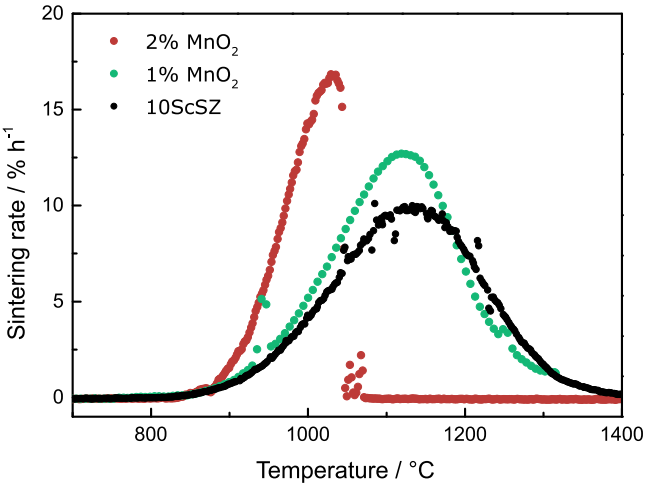


**Fig. 1.** Sintering rate determined by dilatometry for 10ScSZ with addition of 0, 1 and 2mol% $MnO_2$.

Fig. 2 presents SEM images of 2% mol $MnO_2$ doped 10ScSZ sintered at 1250 °C for 5, 10 and 20 h. There is a slight increase in the overall grain size with increased sintering time, but in general the microstructure is comparable for all samples with a high degree of densification and grain sizes in the range of 3–5 µm. Furthermore, the images show areas with a high concentration of twin boundaries that are typically associated with a strain-induced martensitic phase transformation found in 10ScSZ [8]. Larger areas with twin defects are observed for the samples prepared with shorter sintering times.

### 3.2. Role of Mn dopant in ScSZ

In order to evaluate the structural and chemical stability of the materials, several thermal cycles were conducted between room temperature and 800 °C in oxidizing (air, 24 h) and reducing conditions (wet 5% $H_2$, 24 h) on 1MnScSZ and 2MnScSZ pellets. Several samples were studied to obtain representative results. Interestingly, all samples appeared dark after sintering in air, whereas they became white/yellow after annealing in reducing conditions. Upon re-annealing in oxidizing conditions, the pellets reverted to a dark colour. This colour change is associated with a change in the room temperature crystal structure, as will be discussed further below.

To elucidate the predominant valence state of Mn in the fluorite 10ScSZ structure under oxidizing and reducing conditions, a combination of XPS and DFT was employed. As sintered (air, 1250 °C, 10 h) and reduced (wet 10% $H_2$, 900 °C, 48 h) samples of 2MnScSZ were characterised by XPS. To distinguish between surface and bulk properties, several areas were analysed. Freshly fractured cross-sections were analysed to reflect the bulk chemistry of the pellets, while pellet surfaces and powders were used to analyse the surfaces and grain boundaries. Fig. 3 shows examples of the fitted Mn $2p_{3/2}$ peaks for different analysed areas, while

Table 1 summarizes the calculated valence state and concentration of manganese for all analysed positions. Within the bulk of the 2MnScSZ pellets, manganese is predominantly present as $Mn^{2+}$ in both the oxidized and reduced samples. Quantification of the Mn content yielded a concentration of 2mol% in line with the nominal doping concentration. For the powder and surface analyses, however, both the concentration and average valence state were markedly higher than within the bulk, indicating an accumulation

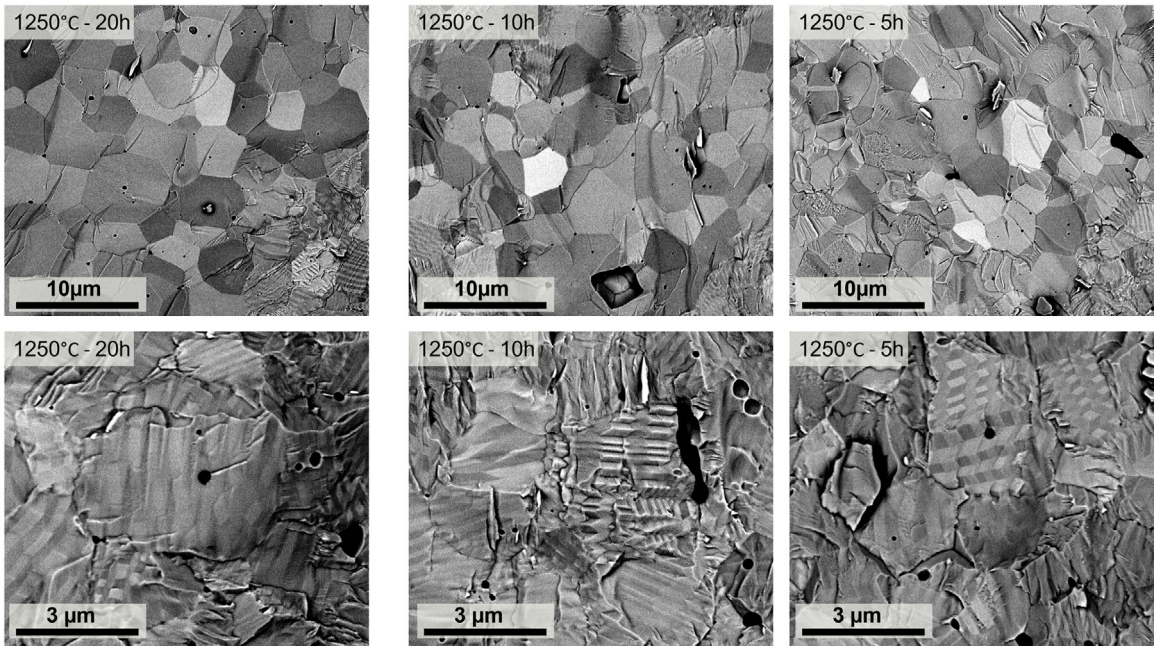


**Fig. 2.** SEM images in cross-section view (fractured surface) of 2MnScSZ samples sintered at 1250 °C for 5, 10 and 20 h.

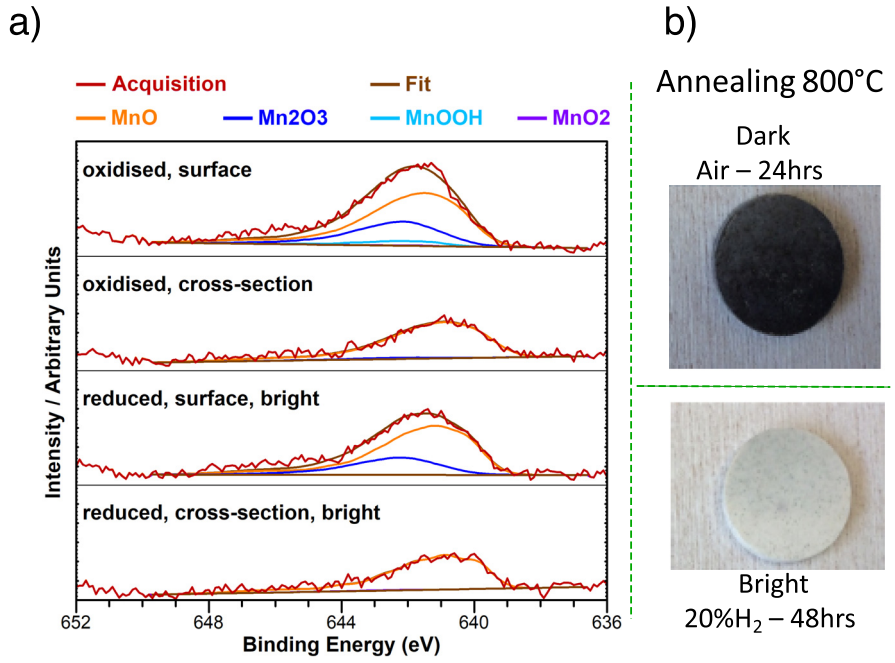


**Fig. 3.** (a) XPS spectra showing the $Mn2p_{3/2}$ peak for selected positions on an oxidized (dark) and reduced sample (bright) as shown in the image (b). Experimental spectra from pure compounds are used for the fitting [23].

of mixed-valence Mn at the surfaces and grain boundaries of 2MnScSZ.

For the reduced samples – which displayed some dark and some bright areas – there was no observable difference in the XPS results that could explain any colour difference.

DFT calculations were used to investigate the electronic structure and valence state of Mn in the cubic $ZrO_2$ structure under equilibrium conditions as a function of temperature and $pO_2$. The $Mn^{4+}$, $Mn^{3+}$ and $Mn^{2+}$ valence states were considered, and the respective Mn–O bond lengths were 2.09 Å, 2.16 Å and 2.26 Å, compared to 2.18 Å for Zr–O. The electronic structure of Mn in the different valence states is shown in Fig. 4. The Mn 4d states were unoccupied for $Mn^{4+}$, partly occupied for $Mn^{3+}$ and fully occupied for $Mn^{2+}$. Similar results were obtained for Mn associated with a single, fully ionized oxygen vacancy.

Based on the thermodynamic transition levels, $Mn^{3+}$ was found to be unstable relative to $Mn^{2+}$ and $Mn^{4+}$. The transition level between these charge states, $\varepsilon(+4/+2)$, was 1.08 eV above the valence band maximum, in accordance with filling of the Mn 4d states (Fig. 4). In comparison, the equilibrium Fermi level as determined from the predominant charge neutrality condition, $[\ddot{v}_O] = 2[Sc'_{Zr}]$, was significantly higher under both reducing and oxidizing conditions in the relevant temperature range. For instance, the equilibrium Fermi level was 2.5 eV and 3.5 eV above the valence

**Table 1**
Calculated average valence state and concentration of manganese for oxidized and reduced 2Mn-ScSZ.

| Condition | Sample Area | Representing | Colour | Mol% Mn | Mn valence |
|---|---|---|---|---|---|
| Reduced | Surface | surface | Bright | 7.2 | 2.2 |
| | Surface | surface | Dark | 1.9 | 2.0 |
| | Cross-section | bulk | Bright | 2.2 | 2.0 |
| | Cross-Section 2 | bulk | Dark | 1.9 | 2.1 |
| | Powder | surface/grain boundary | Bright | 7.2 | 2.4 |
| Oxidized | Surface centre | surface | Dark | 6.6 | 2.3 |
| | Surface edge | surface | Dark | 5.9 | 2.4 |
| | Cross-section | bulk | Dark | 2.3 | 2.0 |
| | Cross-Section 2 | bulk | Dark | 2.6 | 1.9 |
| | Powder | surface/grain boundary | Dark | 6.1 | 2.5–2.7* |

* Some charging was observed during the analysis of the oxidized powder, resulting in an increased uncertainty in the calculated Mn valence state for this specific sample.

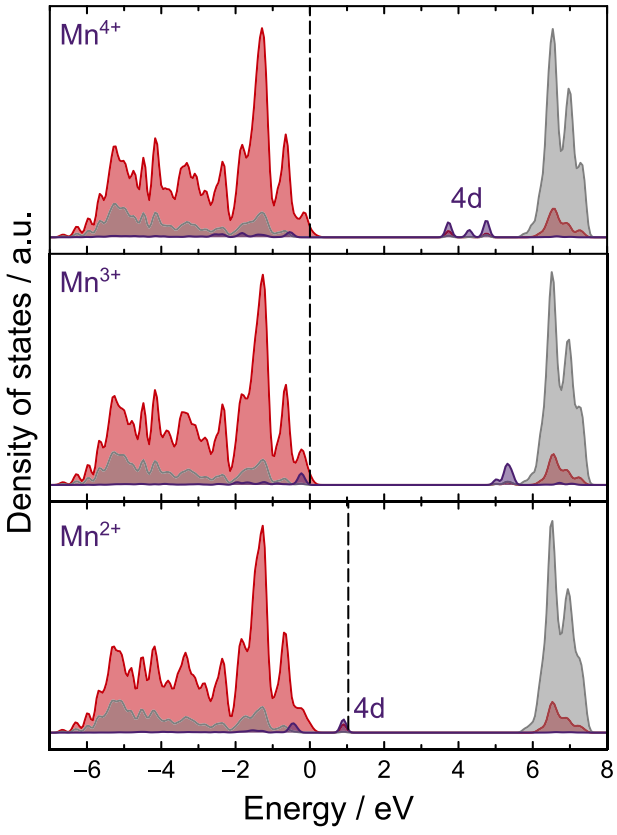


**Fig. 4.** Electronic density of states for $Mn^{4+}$, $Mn^{3+}$ and $Mn^{2+}$ in cubic $ZrO_2$. The valence band maximum is referenced to 0 eV and the dashed line represents the highest occupied states. The valence band consists primarily of O-states (red) and the conduction band consists mainly of Zr-states (grey).

band maximum at 800 °C for a $p_{O_2}$ of 0.21 and $10^{-20}$ bar, respectively. Accordingly, Mn can be expected to predominately exist as $Mn^{2+}$ ($Mn''_{Zr}$) under all conditions relevant to the experiments.

The $Mn^{2+}$ ground state attained a high spin $4d^5$ electron configuration (Fig. 5a). Association between $Mn^{2+}$ and hole polarons was investigated, but hole polarons could not be localised on adjacent oxide ions even if local distortions were introduced. Hole polarons could only be localised adjacent to zirconium vacancies ($v'''_{Zr}$) as shown in Fig. 5b, containing three-fold coordinated oxygen similar to hole polarons in monoclinic $ZrO_2$ and $HfO_2$ [27].

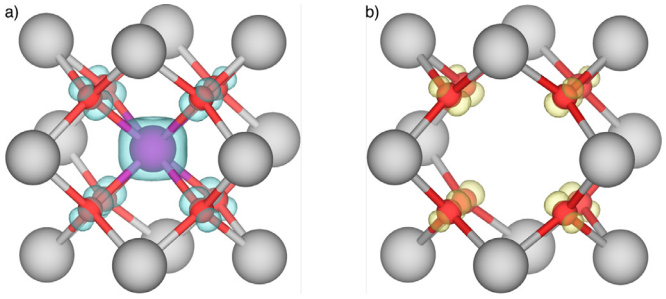


**Fig. 5.** Relaxed structure of $Mn^{2+}$ and the associated charge density isosurface of the five parallel spin states (a) and relaxed structure of a hole polaron localized on oxide ions adjacent to a zirconium vacancy ($v'''_{Zr} \cdot O^{\bullet}_{O}$) (b).

### 3.3. Crystal structure

The crystal structure at room temperature of Mn-doped ScSZ pellets sintered at 1250 °C and 1500 °C was investigated by XRD and subsequent Rietveld refinement to quantify the fraction of cubic and rhombohedral phases. Results are summarized in Table 2. The cubic phase fraction at room temperature increased with increasing sintering temperature for the compositions with low Mn content (0.5–2 mol%). There was no evidence of secondary phases for any of the investigated compositions from the XRD analysis.

The obtained unit cell volumes are slightly lower than values reported in literature for 10ScSZ (32.99 Å) [28], which could be expected to increase when solely comparing the larger ionic radius of $Mn^{2+}$ (0.96 Å) compared to $Zr^{4+}$ (0.84 Å) in an 8-fold coordination. Moreover, the unit cell volume of the cubic polymorph remained essentially unchanged upon increasing Mn content. This is consistent with several reports on Mn-doping in $ZrO_2$, where small amounts of Mn-doping (<3 mol%) results in a decreased lattice parameter, with only minimal effect of higher dopant amounts [20,29,30]. While this lack of volume change may also indicate limited solubility of Mn in ScSZ, there were no observations of any secondary phases in all compositions examined by XRD and SEM. This is also consistent with reported solubilities in YSZ where secondary phase formation was only observed for Mn concentrations above 15 mol% [15,29]. However, we cannot exclude that some excess Mn is either present as a minor secondary phase below the detection limit for XRD/SEM or is accumulated in the grain boundaries. We also note that the composition with 4 mol% Mn does not follow the observed trend in terms of its cubic weight fraction at room temperature for the pellets sintered at 1250 °C. This discrepancy may be related to a non-homogeneous distribution of the mixed powders prior to the reactive sintering, but this has not been elaborated further.

**Table 2**
Weight fractions and unit cell volumes of the cubic and rhombohedral polymorphs at room temperature calculated from XRD diffractograms of sintered pellets produced from dry-mixed powders.

| Mn (mol%) | 1250 °C – 5 h | | | | 1500 °C – 5 h | | | |
|---|---|---|---|---|---|---|---|---|
| | Cubic | | Rhombohedral | | Cubic | | Rhombohedral | |
| | Wt% | Vol. (Å$^3$) | Wt% | Vol. (Å$^3$) | Wt% | Vol.(Å$^3$) | Wt% | Vol. (Å$^3$) |
| 0.5 | 0.12 | 32.86 | 0.88 | 33.04 | 0.13 | 32.86 | 0.87 | 33.04 |
| 1 | 0.21 | 32.82 | 0.79 | 32.99 | 0.59 | 32.85 | 0.41 | 33.03 |
| 2 | 0.86 | 32.85 | 0.14 | 33.06 | 1 | 32.84 | 0 | – |
| 4 | 0.61 | 32.83 | 0.39 | 33.02 | | | | |
| 6 | 0.95 | 32.85 | 0.05 | 32.96 | | | | |
| 10 | 0.95 | 32.87 | 0.05 | 32.92 | | | | |

**Table 3**
Calculated weight fractions of the cubic and rhombohedral polymorph after sintering 2Mn-ScSZ in air at 1250 °C for 5, 10 and 20 h. The same specimen was used for the pellet surface and crushed pellet analysis. All pellets were produced by wet ball milling.

| Sintering time (hours) | Pellet surfaces | | Crushed pellets | |
|---|---|---|---|---|
| | Cubic | Rhombohedral | Cubic | Rhombohedral |
| 5 | 1.00 | 0 | 0.55 | 0.45 |
| 10 | 1.00 | 0 | 0.60 | 0.40 |
| 20 | 1.00 | 0 | 0.68 | 0.32 |

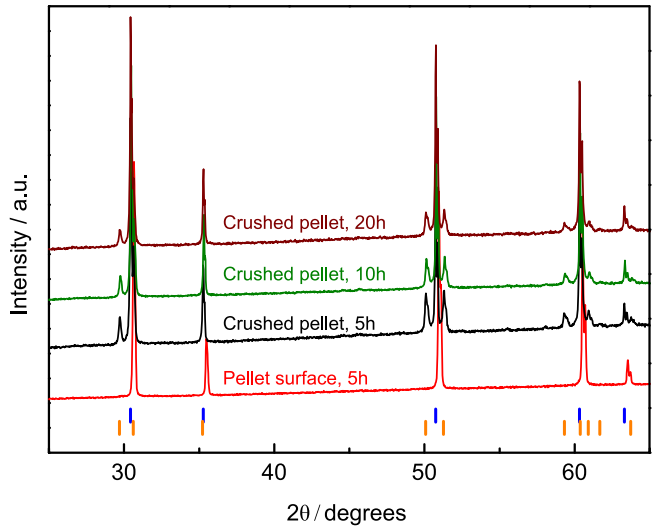


**Fig. 6.** XRD diffractograms of crushed 2MnScSZ pellets after sintering in air at 1250 °C for 5, 10 and 20 h, and a pellet surface after sintering for 5 h showing only the cubic polymorph. All pellets were produced by wet ball milling. The hkl-ticks on the bottom indicate cubic (blue) and rhombohedral (orange) symmetry.

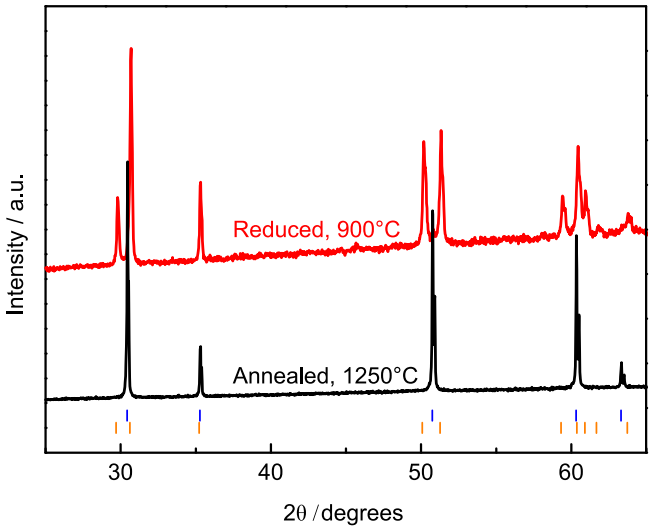


**Fig. 7.** XRD patterns for 2Mn10ScSZ non-compacted powders, annealed in air at 1250 °C and post-reduced in 5% $H_2$ at 900 °C. The hkl-ticks on the bottom indicate cubic (blue) and rhombohedral (orange) symmetry.

The XRD results provided in Table 2 were taken on the surface of the as-sintered pellets. Fig. 6 shows diffractograms of a 2MnScSZ pellet sintered at 1250 °C and of the powder obtained by crushing the same pellet. Comparing these results shows that a significant proportion of the rhombohedral phase is present in the powder while the pellet surface only shows peaks corresponding to the cubic phase. This suggests that there is a difference in the crystal structure between the pellet surface and the bulk interior of the pellet. Table 3 compares the weight fraction of the cubic phase at room temperature for 2 mol% Mn-doped ScSZ sintered at 1250 °C for 5, 10 and 20 h. The cubic fraction increases from 55% to 68% within the bulk interior (denoted crushed pellet) by increasing the sintering time from 5 to 20 h. The calculated (pseudo) cubic lattice parameter was 3.596 Å for the cubic phase and 3.641 Å for the rhombohedral phase independent of the sintering time.

As explained earlier, the pellets analysed in Table 2 were made from dry-mixed powders, whereas the pellets and powders analysed in the following figures and tables (Figs. 6–7 and Table 3) were made from wet ball-milled powders. The latter resulted in a fully stabilised cubic structure at room temperature for all pellets prepared with 2 mol% $MnO_2$, likely due to a more homogeneous distribution of $MnO_2$ in the green pellets before sintering.

An additional experiment was carried out where non-compacted reactive powder mixtures corresponding to 2Mn-10ScSZ were annealed in air at 1250 °C for 5 h, resulting in a fully cubic phase at room temperature (see Fig. 7). This further suggests that a kinetic restriction associated with access to the atmosphere limits the dissolution of $MnO_2$ within the pellet interior during sintering. The 2Mn10ScSZ powder was subsequently annealed and cooled in reducing conditions (humidified 5% $H_2$) at 900 °C for 24 h, which was accompanied by a change in the room temperature structure to a 93% rhombohedral phase as shown in Fig. 7. Similar results were obtained when annealing a sintered pellet (not shown). Both powders and pellets changed colour from dark to bright after annealing in reducing conditions.

HT-XRD was further employed to investigate the phase transitions and thermal expansion of 1MnScSZ and 2MnScSZ in ox-

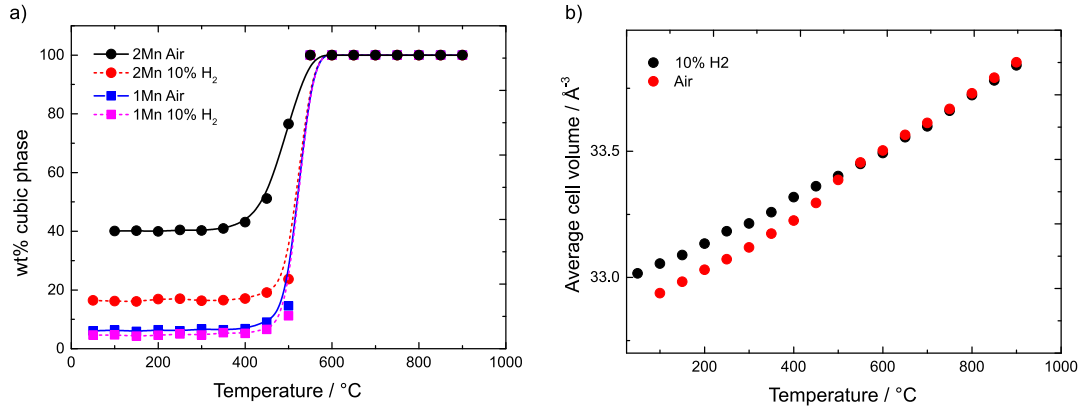


**Fig. 8.** HT-XRD data of 10ScSZ doped with 1% and 2% $MnO_2$ recorded in air and 10% $H_2$ showing the extracted cubic weight fraction (a) and the average cell volume as a function of temperature for 2MnScSZ (b). All measurements are on a powder obtained from crushed pellets sintered at 1250C for 5 h.

**Table 4**
CTEs extracted from HT-XRD and dilatometry in air and wet 10% $H_2$ for 1MnScSZ and 2MnScSZ.

| | CTE in Air ($10^{-6}$ $K^{-1}$) | | | CTE in 10% $H_2$ ($10^{-6}$ $K^{-1}$) | | |
|---|---|---|---|---|---|---|
| Mn (mol%) | 100 °C-900 °C (HT-XRD) | 550 °C-900 °C (HT-XRD) | 550 °C-900 °C (dilatometry) | 100 °C-900 °C (HT-XRD) | 550 °C-900 °C (HT-XRD) | 550 °C-900 °C (dilatometry) |
| 2% | 10.5 (11.9*) | 11.2 | 10.6 | 9.7 | 11.2 | 10.7 |
| 1% | 9.6 | 11.7 | | 9.8 | 12 | |

*Specific CTE for the cubic phase from HT-XRD for 2MnScSZ in air.

idizing and reducing conditions. This analysis was done using crushed pellets based on dry-mixed powders sintered at 1250 °C for 5 h. Diffractograms were recorded every 50 °C upon cooling from 900 °C, and the calculated weight fractions of the cubic and rhombohedral phases are presented in Fig. 8. The onset of the phase transition occurs at 550 °C for both compositions in both oxidizing and reducing conditions. For the 1% Mn-doped composition, there is no significant difference in the extent of phase transition between oxidizing and reducing conditions, whereas the 2%-doped composition retains a higher fraction of the cubic phase upon cooling in oxidizing conditions.

Table 4 presents the coefficients of thermal expansion (CTE) extracted from the HT-XRD data and dilatometry measurements in two different temperature intervals (100–900 °C and 550–900 °C). The CTEs of 2MnScSZ are slightly higher those reported for the cubic phase of 10ScSZ in air (10.3–10.6 $10^{-6}K^{-1}$, 50–800 °C) [10,31], indicating that Mn contributes to an increased thermal expansion of the ScSZ structure. It is also noteworthy to highlight that the CTEs are similar in both oxidizing and reducing atmospheres.

### 3.4. Conductivity

The conductivity of all compositions that effectively stabilised the cubic polymorph at room temperature was characterized to investigate the effect of Mn content and sintering time. Fig. 9 presents an example of a Nyquist plot of 2MnScSZ sintered at 1250 °C for 20 h measured in 20% $H_2$ at 525 °C. The bulk and grain boundary resistances for each measurement were extracted through an equivalent circuit modelling as illustrated in Fig. 9. The bulk resistance was extracted from the high-frequency intercept with the origin, while the grain boundary resistance was modelled with a ($R_{gb}$//$CPE_{gb}$) element. Charge transfer (c.t.) and mass transfer (m.t.) processes attributed to the electrodes were also incorporated in the complete equivalent circuit to accurately describe the complete impedance spectra. All measurements were conducted in a two-point four-wire configuration to avoid any impact of the measurement leads. The bulk conductivity here reflects only the crystalline lattice, the grain boundary conductivity reflects the inverse of the extracted grain boundary resistivity, and the total conductivity reflects the conductivity of the complete polycrystalline ceramic.

Fig. 10 presents the bulk conductivity measured in air for 2, 4 and 10 mol% Mn-doped 10ScSZ sintered at 1250 °C for 5 h as a function of the inverse temperature, in the temperature range 900–550 °C. While 2Mn10ScSZ presents a conductivity fairly similar to the one reported in the literature for 10ScSZ [12,13,32], increasing Mn content above 2% clearly resulted in a decreased conductivity at all temperatures. This was also accompanied by a minor increase in the activation energy, from 77 ± 2 kJ/mol for 2MnScSZ to 82 ± 4 kJ/mol for 10MnScSZ, which is slightly higher than the activation energy reported for Mn-free 10ScSZ (~60–70 kJ/mol) [2,9,10,12,33].

For all compositions there was essentially no difference in the conductivity measured in air, $N_2$ or humidified 20% $H_2$, as illustrated for 2MnScSZ in Fig. 10b. This indicates that the conductivity remains predominantly ionic even with the addition of up to 10 mol% Mn-dopant. This is consistent with the XPS and DFT results showing that Mn remains $Mn^{2+}$ in the fluorite structure with little affinity to generate or stabilize electrons or electron hole polarons.

The impact of sintering time on the conductivity of 2MnScSZ is illustrated in Fig. 11, which compares the bulk and grain boundary conductivity for pellets sintered for 5, 10 and 20 h. The bulk conductivity is essentially constant with the sintering time, albeit slightly higher after 5 h of sintering. Moreover, there is no indication of any phase transformation in 2MnScSZ as otherwise evidenced by a sudden change in the conductivity around 550 °C in 10ScSZ. For all compositions, the bulk conductivity remains identical between oxidizing and reducing conditions, whereas the grain boundary conductivity is significantly decreased with increased sintering time. The latter cannot be rationalised based on any microstructural effects as there are only minor differences in the grain sizes for the different pellets.

Interestingly, the grain boundary conductivity is also significantly increased in reducing conditions, as compared to oxidizing conditions. This can be seen in Fig. 11c, which compares the grain

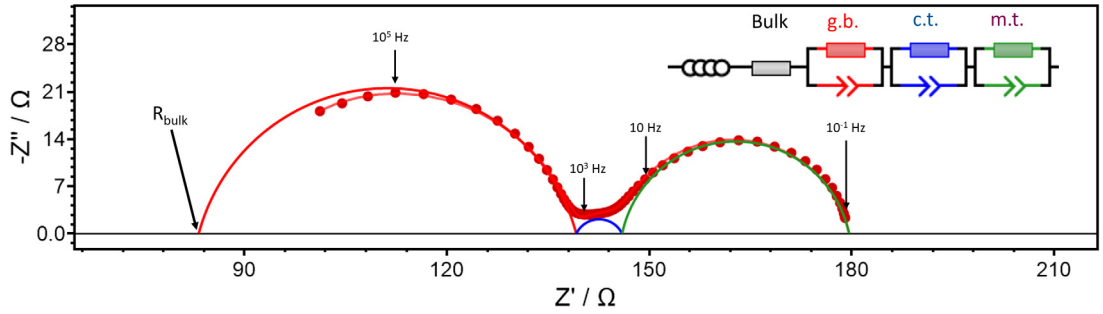


**Fig. 9.** Example Nyquist plot of Mn2ScSZ measured in 20% $H_2$ at 525 °C. The red solid line represents the fit obtained using the equivalent circuit model portrayed in this figure. The red, blue and green semi-circles illustrate the relative resistance contributions from grain boundary, charge transfer (c.t.) and mass transfer (m.t.) processes, respectively. The bulk resistance was extracted from the estimated intercept, as indicated in the figure.

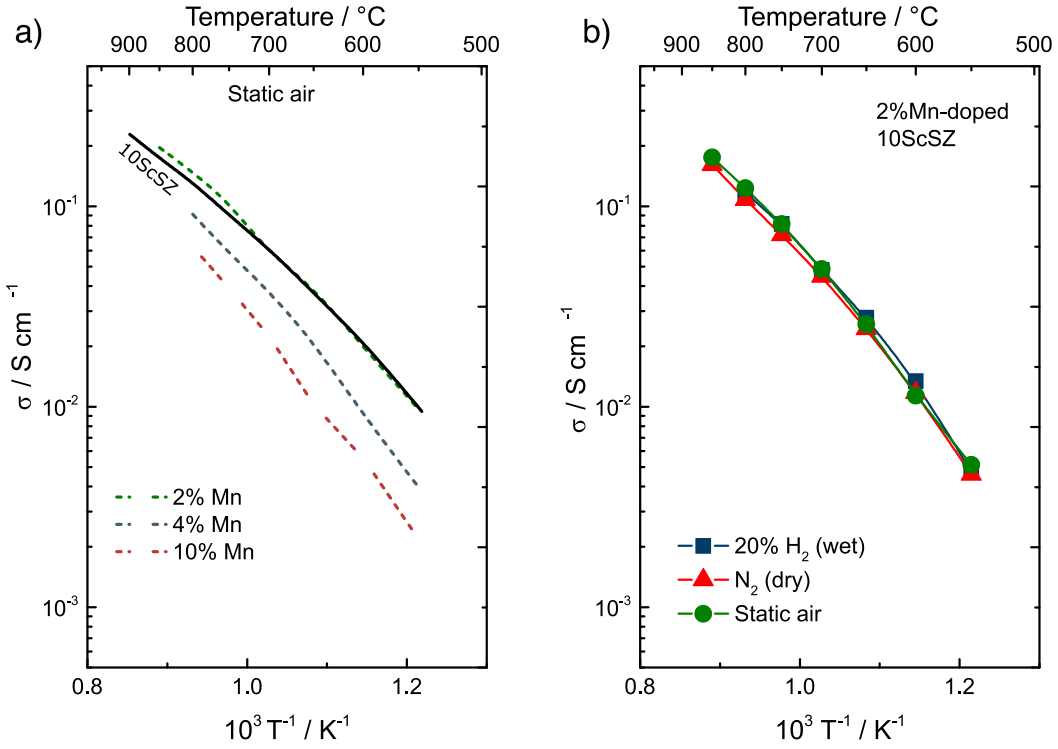


**Fig. 10.** (a) Conductivity of 10ScSZ co-doped with 2, 4 and 10 mol% $MnO_2$ measured in air as a function of inverse temperature. Conductivity of 10ScSZ from literature [13] is also indicated for comparison. (b) Conductivity of 2MnScSZ measured in air, $N_2$ and 20% $H_2$ as a function of inverse temperature.

boundary conductivity for 2MnScSZ measured in air and in wet 20% $H_2$. The grain boundary conductivity is enhanced by almost one order of magnitude by switching from oxidizing to reducing conditions.

The long-term stability in fuel cell conditions was also evaluated for the 2MnScSZ electrolyte composition sintered at 1250 °C for 5 h. The pellets – with Pt/ScSZ electrodes as both cathode and anode – were exposed to synthetic air on the cathode side and humidified 20% $H_2$ in Ar on the anode side at a constant temperature of 800 °C. Fig. 12 presents the total conductivity of one tested over 550 h. As it can be seen, there is an initial drop in conductivity over the first 50 h from 125 to 115 mScm$^{-1}$, after which the conductivity stabilizes at about 115 mScm$^{-1}$. This is followed by a linear degradation over the remaining 500 h of approximately 2%/khr. It should be noted that the electrode polarisation resistance of the Pt-ScSZ electrodes increased significantly over the same interval (see inset Fig. 12). This may influence the interpretation of the ohmic resistance – extracted from the intercept with the origin of the Nyquist plot – due to an increased contribution from the electrode impedance also at higher frequencies. Nevertheless, considering this value as the worst-case scenario, the observed conductivity degradation for 2MnScSZ in this study is significantly lower than the reported degradation rates for 10ScSZ and 1Ce10ScSZ of 15–30%/khr and 5–25%/khr, respectively [3,6,32–34].

## 4. Discussion

### 4.1. Dissolution of manganese

Combined results from XPS and DFT analyses reveal that manganese predominantly exists in its $Mn^{2+}$ state, irrespective of both temperature and $pO_2$, in line with expectations based on the ionic radii for the different manganese valence states. Moreover, electrical measurements reveal no change in electronic conductivity due to formation of electronic charge carriers. Accordingly, the predominant dissolution reactions of $MnO_2$ or $Mn_2O_3$ into the zirconia structure can be written as:

$$MnO_2 \rightarrow Mn''_{Zr} + O_O^x + \ddot{v}_O + \frac{1}{2}O_2(g) \quad (4)$$

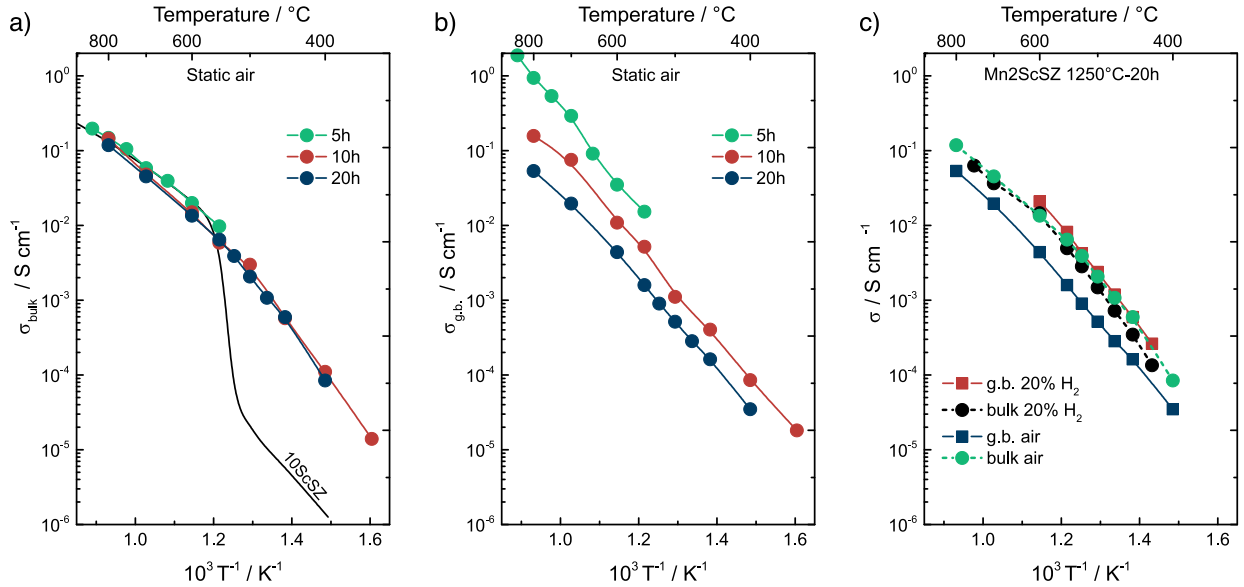


**Fig. 11.** Bulk (a) and grain boundary (b) conductivities of 2MnScSZ sintered at 1250 °C for 5, 10 and 20 h measured in air. c) Comparison of bulk and grain boundary conductivity measured in air and 20% $H_2$ for 2MnScSZ sintered for 20 h.

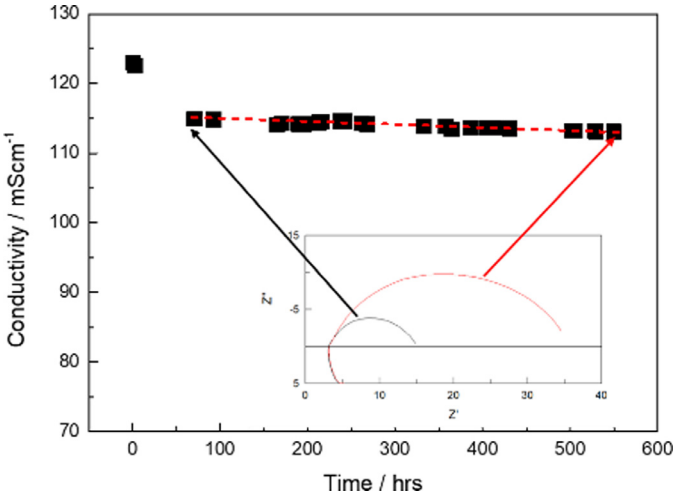


**Fig. 12.** Long-term stability of 2MnScSZ in fuel cell conditions at 800 °C.

$$Mn_2O_3 \rightarrow 2Mn''_{Zr} + 2O_O^x + 2\ddot{v}_O + \frac{1}{2}O_2(g) \quad (5)$$

From these reactions, it is evident that the dissolution of manganese involves a redox reaction and evolution of oxygen gas, indicating that the degree of dissolution will be dependant on the local $pO_2$ during the reaction. This will impact the structure of materials and be regulated by the processing route and densification rate of the pelletized materials. In this work, reactive sintering of the precursor oxides is employed. If dissolution occurs before densification, there should be no difference in the amount of cubic phase for both powder and pellet samples. However, XRD analysis of the non-compacted powders and pellet surfaces for the 2MnScSZ composition revealed a full stabilisation of the cubic phase after sintering for 5 h, whereas the crushed pellets (representing the inner bulk) were only partially stabilised at room temperature (~50wt% cubic). Furthermore, the fraction of the cubic phase in the dense pellets increased with increasing sintering time. This indicates that the dissolution reaction and densification are likely to occur in parallel. The dissolution of $MnO_2$ in the dense inner regions of the pellets may therefore be limited due to restricted release of oxygen gas (and diffusion to the surrounding atmosphere). Thus, the stabilisation process in the inner bulk regions may be kinetically restricted. In contrast, non-compacted powders and near-surface regions of the pellets have unrestricted access to the surrounding atmosphere and thus will not have the same kinetic restriction to the dissolution of $MnO_2$.

### 4.2. Bulk and grain boundary conductivity

It was shown that increasing the Mn content above 2 mol% results in a decreased conductivity at all temperatures, in line with previous work on 10ScSZ where additional acceptor dopants generally results in a decreased oxide ion conductivity [4,35]. The decreased conductivity is accompanied by a slight increase in the activation energy from 77 kJ/mol for 2MnScSZ to 82 kJ/mol for 10MnScSZ. The decreased conductivity and increased activation energy of Mn-doped ScSZ can be attributed to an increased defect association between oxygen vacancies and $Mn^{2+}$ and corresponding increased diffusion barrier [5]. The XRD results revealed that the lattice volume remained essentially unchanged upon increasing Mn content from 0.5% to 10% (Table 2), whereas it would be expected to increase based on the higher ionic radius of $Mn^{2+}$ (0.96 Å) compared to $Zr^{4+}$ (0.84 Å) in 8-fold coordination. The relaxed structures from DFT showed that the Mn–O bond lengths of 8-coordinated $Mn^{2+}$ (2.26 Å) was slightly longer than the Zr–O bond lengths in bulk $ZrO_2$ structure (2.18 Å), while the effect of oxygen vacancies on the bond lengths were not studied in detail. This could indicate an increasing tendency for oxygen vacancy ordering with higher Mn concentrations which would decrease the ionic radius – e.g., for 6-fold coordinated $Mn^{2+}$ the ionic radius is 0.83 Å – comparable to that of $Zr^{4+}$ in an 8-fold coordination. This is consistent with a previous study on Mn-doped $ZrO_2$, where it was found that manganese is predominantly 6-fold coordinated [30]. It may also be impacted by an increased concentration of $Mn^{3+}$ (0.58/0.64 Å in 7-fold coordination) at the higher dopant concentrations – as is previously seen for Mn in YSZ [20,29].

The bulk conductivity of Mn-doped 10ScSZ displayed a negative dependency on Mn-concentration but remained independent of $pO_2$ for all composition, implying a predominantly ionic conductivity even with Mn concentrations up to 10 mol%. This is in

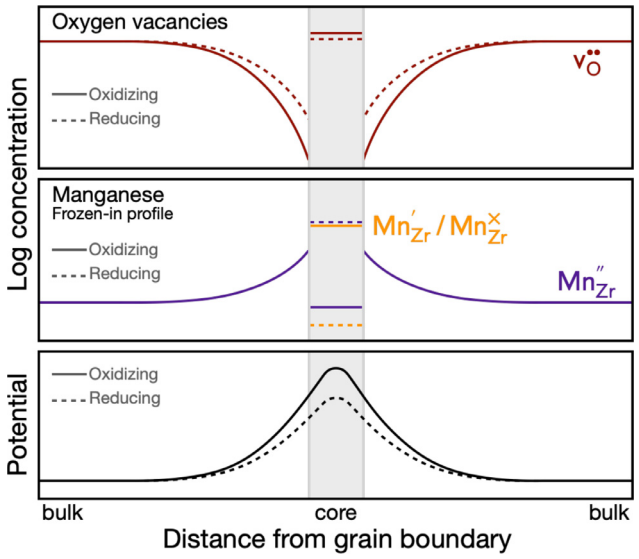


**Fig. 13.** Schematic illustration of concentration and potential profiles across a grain boundary in oxidizing and reducing conditions.

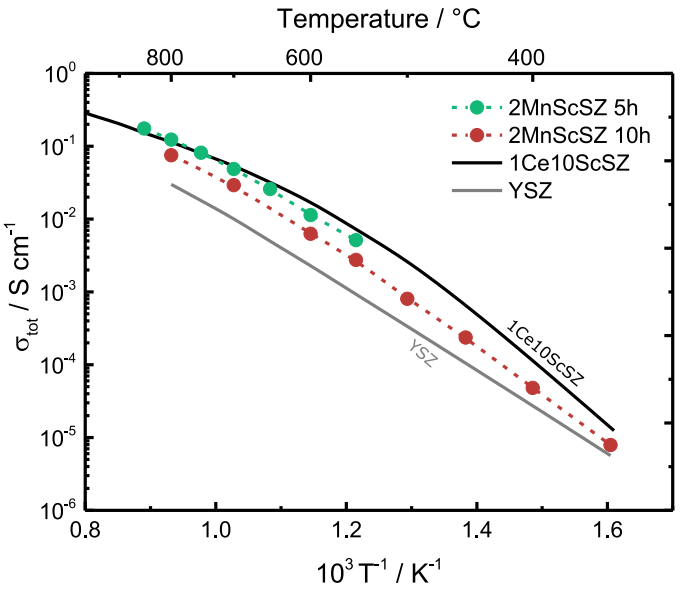


**Fig. 14.** Total conductivity of 2MnScSZ sintered at 5 and 10 h compared to state-of-the-art electrolytes 1Ce10ScSZ [39] and YSZ (in-house data).

line with XPS and DFT results revealing that there are no available redox reactions for Mn within the bulk ScSZ structure. There was, however, a distinct difference in the grain boundary conductivity measured in oxidizing and reducing conditions – with a substantially higher conductivity across the grain boundaries in wet 20% $H_2$. The origin of the grain boundary resistance in acceptor doped zirconia is generally ascribed to a space charge effect arising from an accumulation of positively charged oxygen vacancies in the grain boundary core [36,37]. The accumulated positive charges result in depletion of oxygen vacancies in the space charge region adjacent to the grain boundaries, and thus a lowered oxide ion conductivity across the grain boundaries. Conversely, accumulation of negatively charged defects (such as $Mn'_{Zr}$) within the grain boundary core will counteract the depletion of oxygen vacancies and increase the grain boundary conductivity.

Previous studies have found that co-dopants such as Yb in ScSZ [38] and Mn in YSZ [20] accumulate in the grain boundary core after sintering, in good agreement with our XPS data showing higher Mn-content at the surfaces and grain boundaries compared to bulk. And while the bulk manganese was predominantly $Mn^{2+}$ independent of $pO_2$, the valence state of manganese at the surfaces and grain boundaries of 2MnScSZ changed significantly upon annealing in reducing conditions (average valence state +2) and oxidizing conditions (average valence state +2.4). Contrary to bulk ScSZ where Mn is restricted to the $Mn^{2+}$ valence state, the structurally different grain boundary core is likely to accommodate manganese in other valence states depending on the $pO_2$ and temperature. Accordingly, the observed decrease in grain boundary resistance in reducing conditions may be attributed to the reduction of manganese in the grain boundary core from $Mn^{4+}/Mn^{3+}$ ($Mn^{\times}_{Zr}/Mn'_{Zr}$) to $Mn^{3+}/Mn^{2+}$ ($Mn'_{Zr}/Mn''_{Zr}$) and consequently a reduction of the space charge depletion of oxygen vacancies. A schematic of concentration and potential profiles across a grain boundary in oxidizing and reducing conditions is depicted in Fig. 13, showing higher-valent Mn in the grain boundary core and a larger depletion of oxygen vacancies in the space charge layer under oxidizing conditions. The concentration profile of $Mn''_{Zr}$ is here assumed to be frozen-in at these temperatures (< 800 °C).

These valence changes for manganese at the surfaces and grain boundaries may also explain the observed colour differences upon oxidation and reduction, as $MnO_2$ is predominantly dark in colour, while the more reduced manganese oxides are brighter.

These considerations can further rationalize the observed decrease in grain boundary conductivity upon increased sintering time. Based on the XRD analysis of the cubic stabilisation in 2MnScSZ, an increased sintering time results in more dissolution of Mn into the bulk structure of the sintered pellets and consequently less accumulation of manganese at the grain boundary core. Accordingly, there will be a lower concentration of effectively negatively charged Mn-defects in the grain boundary core for the longer sintering times and a higher depletion of oxygen vacancies within the space charge regions.

We also note that there is a clear presence of twin boundaries in these systems – illustrated in Fig. 2 – that also may impact on the total conductivity. These may potentially act as local heterostructures which in some cases have been shown to exhibit enhanced conductivity along the phase boundary – or they may restrict conductivity across the boundaries due the local distortion of the cubic symmetry. However, the overall effect on the total conductivity remains unclear at the present stage.

### 4.3. Technological relevance and potential

To highlight the relevance of the Mn co-doped 10ScSZ electrolyte, we utilised the state-of-the-art (SOA) 8YSZ as benchmark for its high stability and conductivity at high temperature. As second benchmark is based on the composition 1 mol% $CeO_2$ 10ScSZ exhibiting one of the highest ionic conductivities reported in the literature at intermediate temperature (500–700 °C), albeit presenting some stability challenges when operating in dual atmospheres. In this work, we have shown that the Mn co-doped 10ScSZ compositions fulfil several criteria for achieving a durable and performing thin film electrolyte: the 2MnScSZ electrolyte shows appreciable stability in dual atmosphere and exhibits similar TEC in both oxidizing and reducing atmospheres. The latter are furthermore in the same range than YSZ. This is important to take advantages of the knowledge gained over the past decades on air electrode research, cell's processing and stack development achieved with 8YSZ based cells and stacks. In terms of performance, Fig. 14 illustrates the difference in conductivity as function of temperature for the 2Mn10ScSZ composition, 8YSZ, and 1Ce10ScSZ. The 2Mn10ScSZ electrolyte outperforms the SOA elec-

trolyte over the whole temperature range, and has a similar conductivity than 1Ce10ScSZ at temperature above 600 °C.

## 5. Conclusions

Oxide ion conducting electrolytes of 10ScSZ doped with 1–10 mol% $MnO_2$ were extensively studied with respect to their sinterability, thermal expansion, crystal structure and ionic conductivity. Manganese concentrations above 1 mol% $MnO_2$ were found to effectively limit the phase transition from the highly conducting cubic phase to the less conductive rhombohedral polymorph upon cooling, while enhancing sinterability and densification. Combined DFT and XPS analyses revealed that Mn enters the bulk structure as $Mn^{2+}$, while higher-valent manganese may be present at surfaces and in the grain boundaries. The conductivity of 2MnScSZ was similar to that of 10ScSZ in the temperature range 600 °C-800 °C. Most importantly, the higher conductivity was retained below the phase transition temperature unlike for 10ScSZ. The high ionic conductivity of 2MnScSZ displayed excellent stability towards ageing in fuel cell atmosphere under open circuit. Higher dopant concentrations resulted in lowered ionic conductivity, which was attributed to a higher degree of defect-defect association between $Mn^{2+}$ and oxygen vacancies. The grain boundary conductivity of 2MnScsZ increased with decreasing $pO_2$, which further suggests that redox-active manganese is present in the grain boundary core and affects the space charge depletion of oxygen vacancies.

## Declaration of Competing Interest

The authors declare that they have no known competing financial interests or personal relationships that could have appeared to influence the work reported in this paper.

## Acknowledgements

This project has received funding from the Fuel Cells and Hydrogen 2 Joint Undertaking under grant agreement No 779537. This Joint Undertaking receives support from the European Union's Horizon 2020 research and innovation programme and Hydrogen Europe and Hydrogen Europe Research". Computational resources were provided by Uninett Sigma2 under the project nn9259k. The electrochemical testing was performed using equipment in the High temperature lab of the Norwegian Fuel Cell and Hydrogen Centre supported by The Research Council of Norway (245678).

## References

[1] C. Ahamer, A.K. Opitz, G.M. Rupp, J. Fleig, Revisiting the temperature dependent ionic conductivity of yttria stabilized zirconia (YSZ), J. Electrochem. Soc. 164 (2017) F790.
[2] N. Mahato, A. Banerjee, A. Gupta, S. Omar, K. Balani, Progress in material selection for solid oxide fuel cell technology: a review, Prog. Mater. Sci. 72 (2015) 141–337.
[3] S. Omar, A. Belda, A. Escardino, N. Bonanos, Ionic conductivity ageing investigation of 1Ce10ScSZ in different partial pressures of oxygen, Solid State Ion. 184 (2011) 2–5.
[4] A. Kumar, A. Jaiswal, M. Sanbui, S. Omar, Scandia stabilized zirconia-ceria solid electrolyte (xSc1CeSZ, 5 <x< 11) for IT-SOFCs: structure and conductivity studies, Scr. Mater. 121 (2016) 10–13.
[5] O. Yamamoto, et al., Electrical conductivity of stabilized zirconia with Ytterbia and Scandia, Solid State Ion. 79 (1995) 137–142.
[6] S. Badwal, Scandia–zirconia electrolytes for intermediate temperature solid oxide fuel cell operation, Solid State Ion. 136–137 (2000) 91–99.
[7] E.Z. Santos, R. Muccillo, Single cubic phase Scandia-stabilized zirconia: stabilization and aging at 600°C, ECS Trans. 68 (2015) 421–427.
[8] T. Sakuma, H. Suto, The cubic-to-$\beta$ martensitic transformation in $ZrO_2$-$Sc_2O_3$, J. Mater. Sci. 21 (1986) 4359–4365.
[9] S. Omar, W.B. Najib, W. Chen, N. Bonanos, Electrical Conductivity of 10 mol% $Sc_2O_3$–1 mol% $M_2O_3$–$ZrO_2$ Ceramics, J. Am. Ceram. Soc. 95 (2012) 1965–1972.
[10] S.P.S. Badwal, F.T. Ciacchi, Oxygen-ion conducting electrolyte materials for solid oxide fuel cells, Ionics 6 (2000) 1–21.
[11] A. Azim Jais, et al., Enhanced ionic conductivity of Scandia-ceria-stabilized-zirconia (10Sc1CeSZ) electrolyte synthesized by the microwave-assisted glycine nitrate process, Ceram. Int. 43 (2017) 8119–8125.
[12] W. Preis, et al., Electrical properties of bulk and grain boundaries of Scandia-stabilized zirconia co-doped with yttria and ceria, Solid State Ion. 192 (2011) 148–152.
[13] D.A. Agarkov, et al., Structure and transport properties of melt grown $Sc_2O_3$ and $CeO_2$ doped $ZrO_2$ crystals, Solid State Ion. 322 (2018) 24–29.
[14] M. Chen, B. Hallstedt, L.J. Gauckler, Thermodynamic modeling of phase equilibria in the Mn–Y–Zr–O system, Solid State Ion. 176 (2005) 1457–1464.
[15] K. Yamaji, et al., Effect of Mn-doping on stability of Scandia stabilized zirconia electrolyte under dual atmosphere of solid oxide fuel cells, Solid State Ion. 247–248 (2013) 102–107.
[16] T. Dey, A. Das Sharma, A. Dutta, R.N Basu, Transition metal-doped yttria stabilized zirconia for low temperature processing of planar anode-supported solid oxide fuel cell, J. Alloy. Compd. 604 (2014) 151–156.
[17] M. Shimazu, et al., Stability of $Sc_2O_3$ and $CeO_2$ co-doped $ZrO_2$ electrolyte during the operation of solid oxide fuel cells: part II the influences of Mn, Al and Si, Solid State Ion. 204–205 (2011) 120–128.
[18] M.K. Mahapatra, N. Li, A. Verma, P. Singh, Electrical conductivity of manganese doped yttria (8mol%) stabilized zirconia, Solid State Ion. 253 (2013) 223–226.
[19] T. Kawashima, Phase equilibria in $ZrO_2$–$Y_2O_3$–$MnO_t$ ternary system at 1673 K, Mater. Trans. JIM 40 (1999) 967–971.
[20] H. Li, F.L. Souza, R.H.R. Castro, Kinetic and thermodynamic effects of manganese as a densification aid in yttria-stabilized zirconia, J. Eur. Ceram. Soc. 38 (2018) 1750–1759.
[21] Z. Lei, Q. Zhu, Phase transformation and low temperature sintering of manganese oxide and Scandia co-doped zirconia, Mater. Lett. 61 (2007) 1311–1314.
[22] D.H. Peck, et al., Electrical conductivity of Scandia stabilized zirconia for membranes in solid oxide fuel cells, ECS Proc. 2005–07 (2005) 947.
[23] M.C. Biesinger, et al., Resolving surface chemical states in XPS analysis of first row transition metals, oxides and hydroxides: cr, Mn, Fe, Co and Ni, Appl. Surf. Sci. 257 (2011) 2717–2730.
[24] P.A.W. van der Heide, Multiplet splitting patterns exhibited by the first row transition metal oxides in X-ray photoelectron spectroscopy, J. Electron Spectrosc. Relat. Phenom. 164 (2008) 8–18.
[25] G. Kresse, J. Furthmüller, Efficient iterative schemes for ab initio total-energy calculations using a plane-wave basis set, Phys. Rev. B 54 (1996) 11169–11186.
[26] C. Adamo, V. Barone, Toward reliable density functional methods without adjustable parameters: the PBE0 model, J. Chem. Phys. 110 (1999) 6158–6170.
[27] K.P. McKenna, M.J. Wolf, A.L. Shluger, S. Lany, A. Zunger, Two-dimensional polaronic behavior in the binary oxides m-$HfO_2$ and m-$ZrO_2$, Phys. Rev. Lett. 108 (2012) 116403.
[28] H. Fujimori, M. Yashima, M. Kakihana, M. Yoshimura, Structural changes of Scandia-doped zirconia solid solutions: rietveld analysis and Raman scattering, J. Am. Ceram. Soc. 81 (1998) 2885–2893.
[29] J. Stępień, M. Sikora, C. Kapusta, D. Pomykalska, M.M. Bućko, Local atomic structure evolution in YSZ solid solutions upon Mn doping, Nucl. Instrum. Methods Phys. Res. Sect. B Beam Interact. Mater. At. 411 (2017) 57–62.
[30] A. Fernández-Osorio, L. Ramos-Olmos, C.F. Julián, Black nanocrystalline cubic zirconia: manganese-stabilized c-$ZrO_2$ prepared via the sol–gel method, Mater. Chem. Phys. 147 (2014) 796–803.
[31] F. Tietz, Thermal expansion of SOFC materials, Ionics 5 (1999) 129–139.
[32] T.I. Politova, J.T.S. Irvine, Investigation of Scandia–Yttria–zirconia system as an electrolyte material for intermediate temperature fuel cells—Influence of yttria content in system $(Y_2O_3)_x(Sc_2O_3)_{(11-x)}(ZrO_2)_{89}$, Solid State Ion. 168 (2004) 153–165.
[33] A. Spirin, et al., Scandia-stabilized zirconia doped with yttria: synthesis, properties, and ageing behavior, Solid State Ion. 225 (2012) 448–452.
[34] C. Haering, A. Roosen, H. Schichl, M. Schnöller, Degradation of the electrical conductivity in stabilised zirconia system: part II: Scandia-stabilised zirconia, Solid State Ion. 176 (2005) 261–268.
[35] A. Kumar, A. Jaiswal, M. Sanbui, S. Omar, Oxygen-ion conduction in Scandia-stabilized zirconia-ceria solid electrolyte ($xSc_2O_3$–$1CeO_2$–$(99-x)ZrO_2$, $5 \leq x \leq 11$), J. Am. Ceram. Soc. 100 (2017) 659–668.
[36] X. Guo, R. Waser, Space charge concept for acceptor-doped zirconia and ceria and experimental evidences, Solid State Ion. 173 (2004) 63–67.
[37] R.A. De Souza, E.C. Dickey, The effect of space-charge formation on the grain-boundary energy of an ionic solid, Philos. Trans. R. Soc. Math. Phys. Eng. Sci. 377 (2019) 20180430.
[38] V. Shukla, S. Singh, A. Subramaniam, S. Omar, Long-term conductivity stability of metastable tetragonal phases in $1Yb_2O_3$–$xSc_2O_3$–(99 – $ZrO_2$ (x = 7, 8 mol%), J. Phys. Chem. C 124 (2020) 23490–23500.
[39] D. Lee, et al., Characterization of ZrO co-doped with ScO and CeO electrolyte for the application of intermediate temperature SOFCs, Solid State Ion. 176 (2005) 33–39.